Mechanical Systems and Signal Processing 215 (2024) 111407

Contents lists available at ScienceDirect

Mechanical Systems and Signal Processing

journal homepage: www.elsevier.com/locate/ymssp

Bistable energy-harvesting track nonlinear energy sink in offshore wind turbines

Qinlin Cai [a], Yingyu Hua [b], Songye Zhu [b], Xihong Zhang [c], Haoran Zuo [c,*]

[a] Department of Civil Engineering, Sichuan University, Chengdu, China
[b] Department of Civil and Environmental Engineering, The Hong Kong Polytechnic University, Kowloon, Hong Kong, China
[c] Centre for Infrastructural Monitoring and Protection, School of Civil and Mechanical Engineering, Curtin University, Kent Street, Bentley, WA 6102, Australia

ARTICLE INFO

Communicated by Daniil Yurchenko

Keywords:
Energy harvesting
Vibration control
Bistable track nonlinear energy sink
Offshore wind turbine

ABSTRACT

Energy harvesting is particularly attractive for offshore structures owing to power supply challenges in offshore regions. Offshore structures simultaneously experience substantial vibrations from combined wind-wave loads, thus necessitating structural vibration control. This study investigates the feasibility of a bistable energy-harvesting track nonlinear energy sink (EHTNES) designed for offshore wind turbines (OWTs) to concurrently control vibrations and harvest energy (i.e., a dual-function device). The EHTNES consists of an electromagnetic damper (EMD), a buck-boost energy harvesting circuit (EHC), and a bistable track nonlinear energy sink. The optimal design of the EHTNES is theoretically presented, and the energy-harvesting damping unit (i.e., EMD plus EHC) is validated through the circuit and cyclic tests with the EHC working as an equivalent constant energy-harvesting resistor. Subsequently, the EHTNES is applied to an OWT, and its performances are evaluated under combined wind-wave loads and compared to an energy-harvesting tuned mass damper (EHTMD). Results show that (1) The damping unit simultaneously provides a controllable damping effect and an energy harvesting function; (2) The EHTNES effectively mitigates OWT responses and harvests considerable power into the battery; (3) Compared with the EHTMD, the control effectiveness of the EHTNES experiences a slight degradation but demonstrates superior control robustness and better stable output power when considering stiffness and damping detuning. This study underscores the practicability of the EHTNES for vibration control and energy harvesting in OWTs, thus offering insights into the development of dual-function devices for offshore structures.

1. Introduction

1.1. Energy-harvesting vibration control strategy

The concept of energy-harvesting vibration control originated in automotive engineering during the 1970 s [1]. This approach allows for simultaneous vibration control and energy harvesting, demonstrating the potential for achieving self-powered monitoring and semi-active or active control [2]. In the 2010 s, this concept was expanded to civil engineering and other engineering disciplines with exploration of both electromagnetic (EM) [3–5] and piezoelectric energy transducers [6,7]. The electromagnetic transducer, also

* Corresponding author.
E-mail address: haoran.zuo@curtin.edu.au (H. Zuo).

https://doi.org/10.1016/j.ymssp.2024.111407
Received 23 December 2023; Received in revised form 20 February 2024; Accepted 6 April 2024
Available online 12 April 2024

known as an EM damper (EMD), exhibits a relatively higher mechanical-electro coupling effect and superior power performance than a piezoelectric transducer. Consequently, an EMD is recommended for dual-function devices, especially in large-scale applications [2].

The simplest type of dual-function device is an energy-harvesting EMD (EHEMD) [2]. Zhu et al. [8] considered four different circuits to investigate the damping and power capabilities of an EHEMD. Additionally, the EHEMD has been explored either through numerical simulations or experimental studies in various structural configurations [9–11]. For example, Shen et al. [9] examined the feasibility of an EHEMD in a bridge stay cable, and they found that it functioned as an energy-harvesting viscous damper. Shen et al. [12] and Cai and Zhu [13] experimentally confirmed the effectiveness of an EHEMD in scaled and full-scale bridge stay cables, respectively. Ning et al. [10,14] examined the performance of an EHEMD installed in a seat suspension. Yan et al. [11] utilized an EHEMD as a base isolator for a space antenna reflector and solar panel, effectively damping the second and third vibration modes. The replacement of the conventional damping unit with the EHEMD has led to the development of a series of dual-function devices, including the energy-harvesting tuned mass damper (EHTMD) [15,16] and the energy-harvesting tuned inerter damper (EHTID) [17,18]. Shen et al. [19] conducted a frame experiment with an EHTMD; the harvested energy successfully powered a wireless sensor, achieving self-powered monitoring. Subsequently, they numerically examined the dual-function capabilities of EHTMD in a wind-excited 76-story benchmark building, reporting an output power of 60.7 W at a wind speed of 7 m/s [20]. The application of EHTMD has been extended to various structures, including bridge decks [21], vehicle suspensions [22], space racks [23], and offshore wind turbines (OWTs) [24]. Qian et al. [25] numerically analyzed the dual-function performances of two different EHTIDs installed in an earthquake-excited five-story building. Similar reports on the application of EHTID in earthquake-excited buildings can be found in [26,27].

1.2. Vibration control in OWTs

Offshore structures (mainly platforms and OWTs) experience various environmental loads, such as wind, waves, currents, earthquakes, and ice. Consequently, their vibrations can be more intense and complex, influencing structural serviceability and safety during operations. The vibration control of offshore structures has received extensive attention, and different control methods have been explored, including but not limited to the use of tuned liquid dampers for jacket platforms [28,29], inerter-based vibration isolation systems for floating [30] and jacket [31] platforms, and tuned liquid column dampers for tension leg platforms [32]. Comprehensive reviews on this research topic have been conducted by Kandasamy et al. [33] and Zhang et al. [34]. As OWTs are the objective of this study, only the research on the vibration control of OWTs is reviewed in the following.

Similar passive vibration control devices, including tuned mass dampers (TMDs) [35,36], tuned liquid dampers [37], tuned liquid column dampers [38], their variants (e.g., pendulum and prestressed TMDs [39,40], and inerter-based TMDs [41,42]), cable-based dampers [43] have been reported, albeit not exhaustively, to address the OWT vibration issues. Their effectiveness was demonstrated through numerical simulations and experimental tests. However, passive control devices are often tuned to the target frequency of the protected structure to achieve optimal control effectiveness, implying that passive control devices are effective within a narrow frequency band. If the frequency of control devices deviates from the structural frequency, their effectiveness may highly deteriorate or in certain cases, even amplify the structural responses. As OWTs are increasingly deployed in deep seas with complex seabed conditions and harsh environmental loads, their dynamic characteristics, particularly natural frequency, undergo inevitable changes due to foundation-soil interaction, variations in design and manufacturing, rotor dynamics in operational conditions, material property degradation, and structural damage over their lifetime [44,45]. Previous studies have indicated that TMDs partially lost their control capability for OWTs when considering foundation-soil interaction [46,47].

Nonlinear energy sinks (NESs) emerge as a promising alternative to overcome the narrow effective bandwidth limitation associated with TMDs [48,49]. Unlike TMDs with a linear force–displacement relationship, NESs are distinguished by a nonlinear restoring force, enabling them to work efficiently without specific resonant frequencies. This distinctive property empowers NESs to efficiently mitigate structural vibrations over a wide frequency range, making them robust against frequency variations arising from structures and external excitations.

Previous studies have explored various types of NESs, with recent emphasis on track NESs (TNESs). Wang et al. [50] introduced an NES with a quartic track profile, and a nonlinear force was generated by the NES mass movement along the curved track. However, similar to other NESs, the effectiveness of the TNES is notably contingent on input energy levels and has been proven unsatisfactory. Zuo et al. [51–53] proposed two TNESs with redesigned track profiles. Both TNESs incorporated quadratic and quartic terms in their track profiles: one TNES combined positive quadratic and positive quartic terms (the monostable TNES); the other combined negative quadratic and positive quartic terms (the bistable TNES). Numerical studies were carried out to investigate the control performances of the monostable and bistable TNESs in reducing structural vibrations of OWTs under wind, sea waves, and earthquakes.

1.3. Motivations

The rated power of OWTs is as high as the megawatt level for a single turbine, and the power output of dual-function devices is incomparable with OWTs. However, the primary focus of these devices is to address the challenge of mitigating vibrations of OWTs induced by complex loads in ocean environments, guaranteeing both structural serviceability and safety during their service life. Simultaneously, these devices can harvest a portion of the damping power during the control process. The additional energy-harvesting function would not compromise the vibration control performance, provided an appropriate optimization design is employed. The harvested power here is not intended to increase the total power rating of OWTs, but it can be appreciated in certain scenarios, including (1) facilitating self-powered semi-active or active control, leading to enhanced vibration control performance; (2)

directly powering associated facilities and monitoring sensors located within OWTs, particularly for extreme wind speed conditions wherein OWTs stop working and experience grid outage. Notably, the current power supply within OWTs depends on external grid power rather than using OWTs output power. In this context, the adoption of energy-harvesting technology serves as an internal energy recycling method, somewhat contributing to a reduction in OWT costs without requiring additional external resources.

Although previous research has demonstrated the efficacy of linear dual-function devices in various structures, exploration of nonlinear dual-function devices remains relatively limited. Moreover, given the complex load-induced vibration issues and the challenges in power supply faced by OWTs, dual-function devices become particularly desirable. This study aims to investigate the feasibility of the energy-harvesting TNES (EHTNES) for OWTs subjected to combined wind-wave loads. To the best of the authors' knowledge, this is the first comprehensive investigation into concurrent nonlinear vibration control and energy harvesting within OWTs, offering deep insights into the coupling between OWTs and EHTNES, and advancing nonlinear dual-function devices in offshore structures. The specific works carried out in this study are: (1) A model is developed for a bistable EHTNES consisting of a bistable TNES, an EMD, and an energy harvesting circuit (EHC). (2) Experimental tests are conducted to validate the efficiency of the energy-harvesting damping unit. (3) The vibration control and energy harvesting performances of both EHTNES and EHTMD in OWTs are evaluated and compared. The paper is structured as follows: Section 2 provides a detailed modeling description of EHTNES. Section 3 presents the experimental exploration of the energy-harvesting damping unit. Sections 4 and 5 delve into the 5 MW OWT model and the simulations of wind and wave loads. The numerical results of the OWT equipped with EHTNES are analyzed and compared with EHTMD in Section 6. Section 7 summarizes the conclusions.

2. Bistable EHTNES model

The developed bistable EHTNES is composed of an EMD, an EHC, and a bistable TNES. The EMD serves to introduce a controllable damping effect, converting mechanical energy into electrical energy. The EHC facilitates energy storage, with its characteristics impacting the damping effect of the EMD. Meanwhile, the bistable TNES provides the nonlinear stiffness force. This section elaborates on the intricate modeling of the bistable EHTNES.

2.1. EMD

Fig. 1(a) shows a schematic of an EMD, and its damping c_d is [8],

$$c_d = c_p + c_{em} \tag{1}$$

where c_p and c_{em} are the EMD parasitic and EM damping, respectively. The parasitic damping c_p is contributed by the Coulomb friction and parasitic viscous damping, and it is usually assumed as a constant. The EM damping c_{em} is expressed by

$$c_{em} = \frac{K_{eq}^2}{R_{coil} + R_{load}} \tag{2}$$

where K_{eq} and R_{coil} are the EMD machine constant and coil resistance, respectively; R_{load} is the external load resistance. The EMD coil exhibits both resistance and inductance features. The coil inductance effect is ignored in this study, considering its small value and low-frequency OWT vibrations. However, using a pure resistor circuit cannot harvest energy, and a few EHCs that function as an equivalent resistor have been proposed [13,54].

2.2. EHC

Achieving controllable resistance is a crucial criterion for the EHC in dual-function devices, given its impact on vibration damping. The buck-boost EHC stands out as a promising representative, offering the capability for energy storage while serving as a controllable equivalent resistor. The buck-boost EHC, as shown in Fig. 1(b), has been successfully applied in dual-function devices and tested in

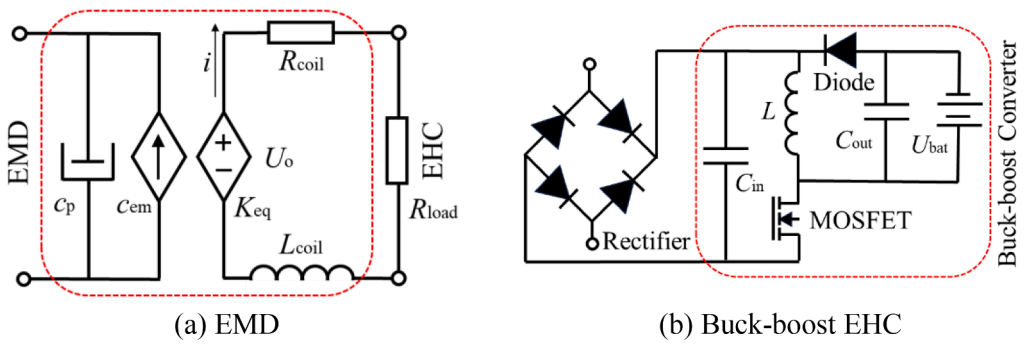

Fig. 1. Modeling of energy-harvesting damping unit.

high-rise building [20], bridge stay cable [13], and high-speed train suspension [55]. It consists of a full bridge rectifier and a typical buck-boost converter with a battery. The rectifier enables the conversion of alternating current to direct current (DC), and the buck-boost converter with a battery is a controllable energy-harvesting equivalent resistor. This buck-boost EHC is adopted in the proposed dual-function devices in this study and briefly introduced herein.

The buck-boost EHC operates in either continuous operation mode (CCM) or discontinuous operation mode (DCM), contingent upon the inductor voltage and circuit characteristics. The EHC operates in DCM when

$$U_{\text{ind}} \leq \frac{1-d}{d}(U_{\text{bat}} + U_{\text{F}}) \tag{3}$$

where U_{ind}, U_{bat}, and U_{F} represent the inductor voltage when the MOSFET is turned on, the battery voltage, and the diode voltage drop, respectively; d is the duty cycle of the pulse-width modulation (PWM) waves for the MOSFET. Cai and Zhu [13] reported that this EHC exhibits equivalent constant resistance characteristics and relatively higher power efficiency in DCM. Consequently, a relatively high-voltage battery is usually employed in the modeling to ensure that the EHC predominantly operates in DCM. The equivalent resistance R_{eq} of the EHC in DCM is

$$R_{\text{eq}} = R_{\text{load}} = \frac{2Lf_{\text{w}}}{d^2} + \frac{R_{\text{on}}}{d} \tag{4}$$

where L is the inductance, f_{w} is the switching frequency of the MOSFET (i.e., PWM frequency), and R_{on} is the on-resistance of the MOSFET. Notably, the rectifier voltage drop-induced equivalent resistance is not considered in the modeling.

2.3. Bistable TNES

The bistable TNES is designed as a hybrid of a quadratic profile and a quartic profile, and it is expressed by a polynomial with both second- and fourth-order terms in mathematics,

$$h(x_{\text{N}}) = a_1 x_{\text{N}}^2 + a_1 x_{\text{N}}^4 (a_1 < 0, a_2 > 0) \tag{5}$$

where h (x_{N}) is the track profile, x_{N} is the TNES mass displacement with respect to the reference, and a_1 and a_2 are track profile coefficients. The nonlinear restoring force F_{N} caused by the mass motions along the curved track can be derived by using the Euler-Lagrange method [50],

$$F_{\text{N}} = m_{\text{N}}\left[\ddot{x}_{\text{N}}(h'(x_{\text{N}}))^2 + \dot{x}_{\text{N}}^2 h'(x_{\text{N}})h''(x_{\text{N}}) + gh'(x_{\text{N}})\right] \tag{6}$$

where m_{N} is the bistable TNES mass. Substituting Eq. (5) into Eq. (6), the nonlinear force F_{N} of the bistable TNES can be rewritten by [51]

$$F_{\text{N}} = m_{\text{N}}\left[\left(2a_1 x_{\text{N}} + 4a_2 x_{\text{N}}^3\right)^2 \ddot{x}_{\text{N}} + \left(2a_1 x_{\text{N}} + 4a_2 x_{\text{N}}^3\right)\left(2a_1 + 12a_2 x_{\text{N}}^2\right)\dot{x}_{\text{N}}^2 + \left(2a_1 x_{\text{N}} + 4a_2 x_{\text{N}}^3\right)g\right] \tag{7}$$

Although the total force F_{N} produced by the bistable TNES is complicated and encompasses three distinct terms, it is dominated by m_{N} ($2a_1 x_{\text{N}} + 4a_2 x3$ N) g when the TNES is exposed to low and moderate external excitations. This finding has been demonstrated in the previous studies [51,52].

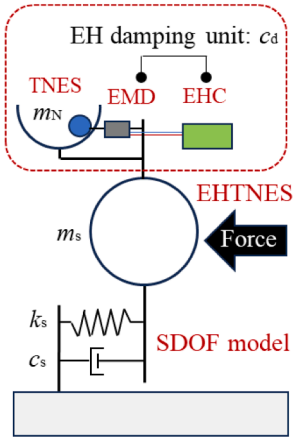

Fig. 2. Schematic of an SDOF-EHTNES system.

2.4. Optimal design

In this subsection, the developed EHTNES is optimally designed. OWT is simplified as a generalized single-degree-of-freedom (SDOF) structure, and its modal mass, natural frequency, and damping ratio will be used. Fig. 2 shows a schematic of an SDOF structure equipped with an EHTNES.

The governing equations of the system under a force excitation are as follows:

$$m_s\ddot{x}_s + c_s\dot{x}_s + k_s x - c_d\dot{x}_N - F_N = F \tag{8}$$

$$m_N\ddot{x}_N + c_d\dot{x}_N + F_N = -m_N\ddot{x}_s \tag{9}$$

where m_s, c_s, and k_s are the structural mass, damping, and stiffness, respectively, c_d is the EHTNES damping coefficient realized by the energy-harvesting damping unit (See Eq. (1)), x_N is the EHTNES mass displacement relative to the structure, and F is the external force excitation. According to the statistical linearization method [56], the nonlinear force of the EHTNES can be estimated in a linear form,

$$F_N \approx m_N\left(2a_1x_N + 4a_2x_N^3\right)g = k_1x_N + k_2x_N^3 = k_Nx_N \tag{10}$$

where

$$k_1 = 2a_1m_Ng \tag{11}$$

$$k_2 = 4a_2m_Ng \tag{12}$$

$$k_N = E\left(\frac{\partial F}{\partial x_N}\right) = k_1 + 3k_2E\left(x_N^2\right) = k_1 + 3k_2\sigma_{x_N}^2 \tag{13}$$

where k_N is the equivalent stiffness, E is the expected value operator, and σ_{xN} is the root mean square (RMS) displacement of the EHTNES mass. Notably, the above linear approximation of the force is only used for the EHTNES design, specifically the stiffness coefficients k_1 and k_2. After obtaining the optimal k_1 and k_2, the nonlinear form of the force (i.e., $F_N = k_1x_N + k_2x_N^3$) is employed in the time-domain analysis (Section 6) for investigating the dual-function performances of the EHTNES.

The external force excitation is assumed to be a zero-mean stationary Gaussian stochastic process with white noise power spectral density S_0 to simplify the EHTNES design, and the RMS responses of the SDOF-EHTNES system can be solved by

$$\mathbf{AC} + (\mathbf{AC})^T + 2\pi S_0\mathbf{BB}^T = 0 \tag{14}$$

where $\mathbf{B} = \{0\ 0\ 1\ 0\}^T$ is the input vector, $\mathbf{C}$ is the response covariance matrix, and $\mathbf{A}$ is the state matrix given by

$$\mathbf{A} = \begin{bmatrix} 0 & 0 & 1 & 0 \\ 0 & 0 & 0 & 1 \\ -\omega_s^2 & \mu\omega_N^2 & -2\xi_s\omega_s & 2\mu\xi_N\omega_N \\ \omega_s^2 & -(1+\mu)\omega_N^2 & 2\xi_s\omega_s & -2(1+\mu)\xi_N\omega_N \end{bmatrix} \tag{15}$$

where $\omega_s = (k_s/m_s)^{1/2}$ and $\xi_s = c_s/(2m_s\omega_s)$ are the structural frequency and damping ratio, respectively, $\mu = m_N/m_s$ is the mass ratio between the EHTNES and the SDOF structure, and $\omega_N = (k_N/m_N)^{1/2}$ and $\xi_N = c_d/(2m_N\omega_N)$ are the frequency and damping ratios of the linearized EHTNES, respectively.

The RMS displacement of the SDOF-EHTNES system (the square root of the first diagonal element in the matrix $\mathbf{C}$) is dependent on k_1 and k_2 (i.e., the track profile coefficients a_1 and a_2) and ξ_N under given μ and S_0. In this study, the optimization is to determine the optimal k_1, k_2, and ξ_N that minimize the RMS displacement of the SDOF structure.

As mentioned above, the EMD plus EHC serves as the EHTNES damping unit. Once the optimal damping $c_{d,opt}$ for vibration control is determined, the designed EHC equivalent resistance can be calculated by

$$R_{eq,vc} = \frac{K_{eq}^2}{c_{d,opt} - c_p} - R_{coil} \tag{16}$$

where $c_{d,opt}$ is the EHTNES optimal damping coefficient for vibration control.

Power efficiency is a standard metric for evaluating the energy harvesting performance of a dual-function device. It is commonly divided into the following three sub-efficiencies:

$$\eta = \frac{P_{em}}{P_d}\frac{P_{rect}}{P_{em}}\frac{P_{out}}{P_{rect}} = \eta_1\eta_2\eta_3 \tag{17}$$

where

$$\eta_1 = \frac{c_{em}}{c_{d,opt}} \tag{18}$$

$$\eta_2 = \frac{R_{eq}}{R_{eq} + R_{coil}} \tag{19}$$

where P_d is the total damping power of the dual-function device, P_{em} is the EM damping power, P_{rect} is the power into the buck-boost converter, and P_{out} is the output power (i.e., the power charged into the battery). Therefore, η_1 represents the ratio of the EM damping power to the total damping power, η_2 denotes the ratio of the electrical power after the rectifier to the EM damping power, and η_3 is the power efficiency of the buck-boost converter. In the dual-function device design, η_3 is typically assumed to be 1 and the bridge rectifier effect is ignored. Zhu et al. [8] derived the corresponding optimal resistance condition for power efficiency,

$$R_{eq,eh} = R_{coil}\left(1 + \frac{K_{eq}^2}{c_p}\right)^{1/2} \tag{20}$$

In this regard, the optimal dual-function performances can be achieved through an appropriate EMD design (i.e., K_{eq}, c_p, and R_{coil}) to ensure $R_{eq,\ vc} = R_{eq,eh}$; however, the mechanical design of EMD is beyond the scope of this study. Once the EMD parameters are given, the EHC parameters are determined to satisfy the on-demand resistance characteristic. The duty cycle enables controlling the EHC resistance feature [12,13], and the optimal duty cycle is calculated as follows:

$$d_{opt} = \frac{4Lf_w}{\left(R_{on}^2 + 8Lf_w\left(\frac{K_{eq}^2}{c_{d,opt} - c_p} - R_{coil}\right)\right)^{1/2} - R_{on}} \tag{21}$$

The optimal design of EHTMD can similarly follow the above steps (not introduced here for conciseness).

3. Experiments on energy-harvesting damping unit

The combination of EMD and buck-boost EHC constitutes the essential component of the EHTNES and EHTMD, referred to as the energy-harvesting damping unit. Circuit and MTS experiments were conducted to provide a brief overview of the equivalent resistance, damping characteristics, and power performance. This experimental investigation establishes a practical foundation for dual-function devices and strongly supports the application of the developed EHTNES.

3.1. Experimental setup

A buck-boost EHC was fabricated and tested in different DC inputs. The EHC component characteristics were calibrated by the RLC meter (model No.: Hioki 3522–50): input capacitance of 680 μF with equivalent series resistance (ESR) of 0.12 Ω, output capacitance of 10 μF with ESR of 0.5 Ω, and inductance of 105 μH with ESR of 0.2 Ω. PWM waves with a fixed duty cycle of 50 % and frequency of 21.6 kHz were generated by a wave generator (model. No.: Keysight 33500B). A 6.5 V rechargeable battery was used, and the DC was inputted from 1 V to 5 V. Therefore, the EHC worked in DCM in the concerned DC range. An oscilloscope (model No.: Tektronix DPO4104B) with voltage probes (model No.: Tektronix TPP0500) and a current probe (model No.: Tektronix TCP0060A) were adopted to record the EHC current and voltage. The sampling frequency was set as 250 MHz, much higher than the switching frequency, to

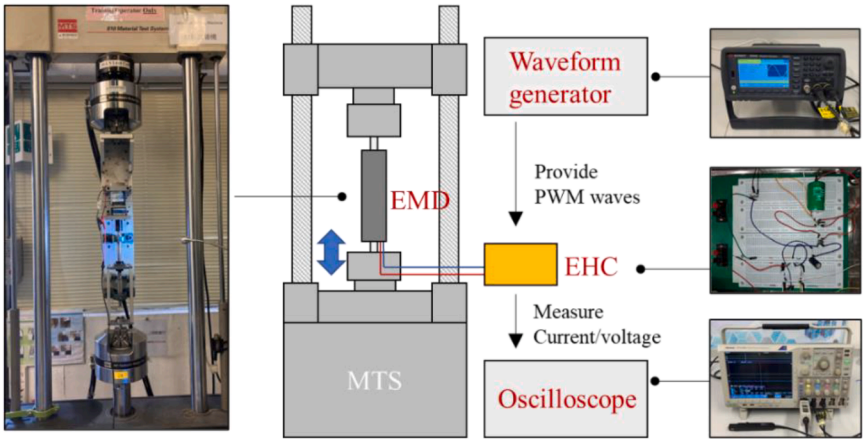

Fig. 3. Experimental setup of the energy-harvesting damping unit for cyclic tests.

accurately record the EHC signal waveforms.

After the circuit tests, the EHC was attached to an EMD to form an energy-harvesting damping unit. Fig. 3 shows the experimental setup, wherein the EMD was the same as that employed by Hua et al. [57]. The tested EMD configuration primarily consists of a rotary EM transducer with a gearbox, a ball screw, and a coupler. The gearbox, ball screw, and coupler construct the typical mechanical transmission system. The ball screw serves to convert linear motion into rotary motion, while the gearbox amplifies the rotation angle of the EM transducer. Additionally, the coupler facilitates the conversion of rotary motion from the ball screw to the EM transducer (Interested readers can refer to [57] for more detailed information on the EMD mechanical design). In the current setup, the estimated parasitic damping c_p was 5 kN·s/m, the coil resistance R_{coil} was 7.5 Ω, and the machine constant K_{eq} was 640 N/A. The damping and power performance of the energy-harvesting damping unit was evaluated through cyclic tests.

3.2. Experimental results

Fig. 4 shows the rectifier current and voltage of the EHC under a DC input of 4 V. The typical triangle current form of the EHC DCM was observed. Upon turning off the MOSFET, the current experienced oscillations induced by resonance stemming from the equivalent capacitance and leakage inductance. Using the average rectifier voltage and current, the equivalent resistance of the EHC was approximated. In Fig. 5(a), the equivalent resistances of the EHC are depicted under various DC inputs. The equivalent resistance remained nearly constant at 23.4 Ω, aligning reasonably well with the theoretical value of 20.2 Ω. The slight discrepancy was attributed to the relatively large ESRs of the electrical components. Fig. 5(b) illustrates the corresponding power performance of the EHC, revealing an output power of up to 0.5 W under a 5 V DC input. These results underscore the effectiveness of employing a DCM buck-boost EHC as an equivalent constant energy-harvesting resistor.

Fig. 6 presents the relationships between force, displacement, and velocity of the energy-harvesting damping unit in 1 Hz and 5 mm cyclic tests. The obtained results closely aligned with theoretical calculations based on a pure resistance of 20 Ω, showcasing a nearly identical damping effect. Specifically, the linear fitting slope of the force–velocity results indicated an overall damping coefficient of approximately 19.7 kN·s/m, closely matching the theoretical damping coefficient of 19.9 kN·s/m with a pure resistance of 20 Ω. The backlashes in the mechanical transmission system led to the observed discrepancies. These fluctuations can be minimized with appropriate mechanical design optimization. The corresponding measured damping power P_d was 9.7 W, and the output power P_{out} was 2.3 W. Notably, under the given harmonic excitation, the EHC partially operated at CCM. These results confirmed the efficacy of the energy-harvesting damping unit, laying a concrete foundation for the dual-function capability of the proposed EHTNES in this study.

4. 5 MW OWT model

The benchmark OWT for this study is the widely utilized NREL 5 MW wind turbine [58] in academia. Fig. 7(a) shows a schematic of the OWT with EHTNES, and Table 1 presents the detailed information of the OWT. As documented [58], the tower's wall thickness is increased by 30 % to ensure that the first eigenfrequency falls within one to three times the rotating frequency across the entire operational range. Moreover, the outer diameter and thickness of the tower exhibit a linear decrease from the base to the top. The tower and monopile are constructed from steel, with steel having a density of 8,500 kg/m^3 and an elastic modulus of 210 GPa [58].

This study aims to design a bistable EHTNES and to investigate its effectiveness in energy harvesting and controlling the tower responses when subjected to stochastic wind and sea wave loads. Therefore, only the tower and monopile are modeled by a multi-degree-of-freedom system using Euler-Bernoulli beam elements. The rotor-nacelle assembly, consisting of three blades, a hub, and a nacelle, is treated as an additional mass with a mass moment of inertia located at the top of the tower.

To balance computational accuracy and efficiency, the tower and monopile foundation are discretized into 22 elements, spanning from the monopile base to the tower top. Several trials were conducted to determine the optimal element lengths, resulting in lengths

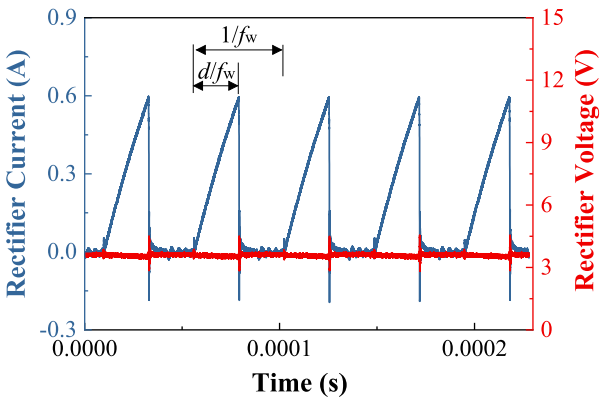

Fig. 4. Experimental rectifier voltage and current under a 4 V DC input.

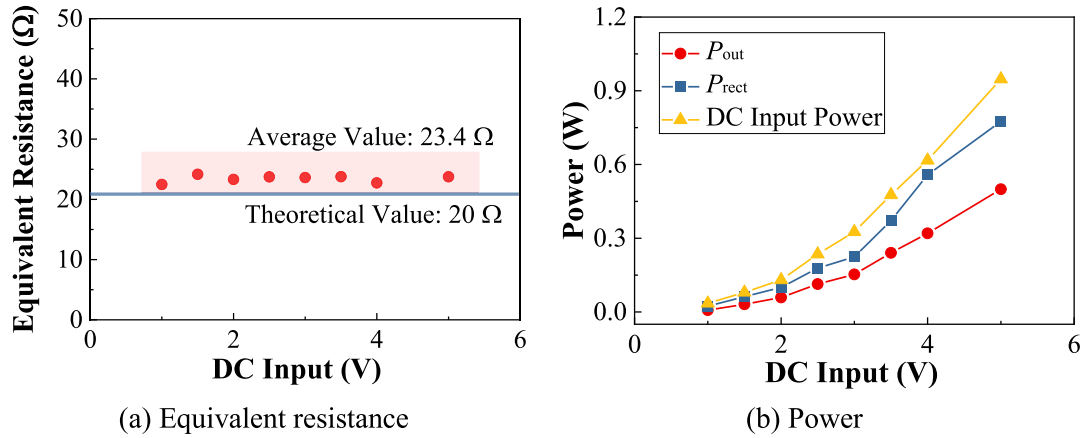

Fig. 5. Equivalent resistance and power of buck-boost EHC under various DV inputs.

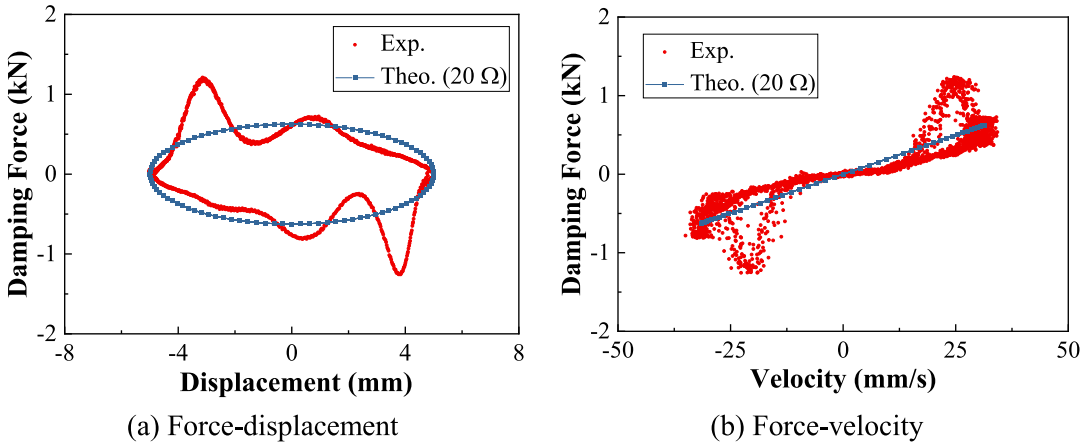

Fig. 6. Force-displacement and −velocity relationships of the energy harvesting damping unit.

of 5 m for the first 21 elements and 2.76 m for the final element. Fig. 7(b) shows the discretization of the OWT. As shown, a total of 44 degrees of freedom (DOFs), including translational and rotational DOFs at each element node, are considered for the OWT without control. Given that the monopile and tower feature hollow and circular cross-sections, the mass and mass moment of inertia at cross-sections and the sectional flexural stiffness along the height of the monopile and tower can be determined on the basis of geometries, material density, and elastic modulus. Subsequently, the mass ($\mathbf{M}_{owt}$) and stiffness ($\mathbf{K}_{owt}$) matrices of the OWT without control are developed. Further details can be found in [59] (they are not introduced here for conciseness).

The first two frequencies of the tower are found to be 0.2810 Hz and 1.9456 Hz, respectively. Rayleigh damping is employed to develop the damping matrix $\mathbf{C}_{owt}$ ($=\alpha\mathbf{M}_{owt}+\beta\mathbf{K}_{owt}$). A damping ratio of 1 % is assigned to the first and second vibration modes of the tower. Consequently, α is 0.0309, and β is 0.0014. The simulated wind and sea wave loads in Section 5 are applied to the corresponding nodes as external excitations.

Furthermore, only the first vibration mode of the OWT is targeted for control; thus, the EHTNES is located at the tower top. For the case of the OWT controlled by the EHTNES, an additional DOF is considered (x_{45} in Fig. 7(b)), and the control force of the EHTNES is applied at the tower top (x_{43} in Fig. 7(b)). Following the formulation of the mass, stiffness, and damping matrices, along with the excitation vector, the governing equation of the OWT controlled by the EHTNES is

$$\mathbf{M}\ddot{\mathbf{X}}+\mathbf{C}\dot{\mathbf{X}}+\mathbf{K}\mathbf{X}=\mathbf{F}+\boldsymbol{\gamma}(F_N+F_d) \tag{22}$$

where $\mathbf{M}=[\mathbf{M}_{owt},0;0,m_N]$, $\mathbf{C}=[\mathbf{C}_{owt},0;0,0]$, and $\mathbf{K}=[\mathbf{K}_{owt},0;0,0]$. $\mathbf{F}$ is the wind-wave loads as presented in Section 5, F_N and F_d are the nonlinear stiffness and damping forces provided by the EHTNES, respectively, $\boldsymbol{\gamma}$ is the location vector of the control force, and $\mathbf{X}=[x_1, x_2, \ldots, x_{45}]$ is the response vector. Notably, x_{43} is the tower top displacement. Similarly, the governing equation of the OWT controlled by the EHTMD can be established (it is not presented here for brevity).

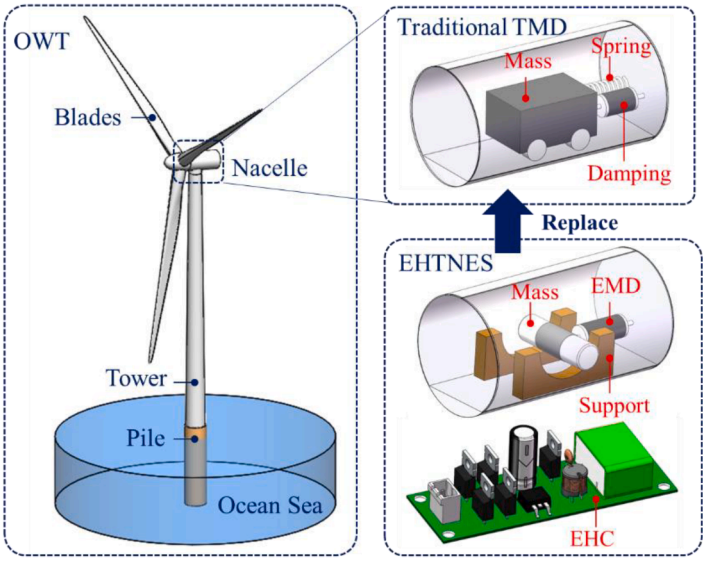

(a) Schematic

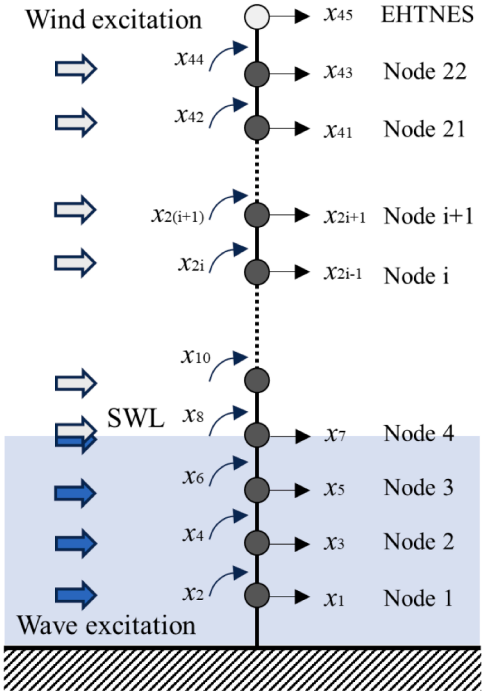

(b) Analytical model (SWL: still water level)

Fig. 7. Schematic and analytical model of the OWT equipped with an EHTNES.

5. Vibration sources

Wind loads on the rotating blades and tower are simulated using the FAST software, wherein the pre-processing module TurbSim generates the wind profile with the Kaimal spectrum and the spatial coherency loss function [60]. Following wind generation, the NREL 5 MW OWT is constructed in FAST, and wind loads are calculated in the internal AeroDyn subroutine using the blade element momentum method [61]. Subsequently, wind load time histories are extracted and applied to the developed model. Given that the blades are not explicitly modeled, the resultant forces and moments at the root of the blades are applied at the tower top.

Table 1
Main parameters of the 5 MW OWT [58].

Parameters	Value	Parameters	Value
Tower height	87.6 m	Cut-in, rated, cut-out wind speeds	3 m/s, 11.4 m/s, 25 m/s
Tower mass	347,460 kg	Hub diameter	3 m
Tower wall thickness	19–27 mm	Hub height	90 m
Tower diameter	3.87–6 m	Hub mass	56,780 kg
Tower structural damping ratio	1 %	Blade second moment of inertia	11,776,047 kg·m^2
Monopile height	20 m	Blade overall mass	17,740 kg
Monopile diameter	6 m	Nacelle mass	240,000 kg
Monopile wall thickness	60 mm		

The effectiveness of the proposed bistable EHTNES is examined under four mean wind speeds: 8 m/s, 11.4 m/s, 16 m/s, and 25 m/s. These speeds fall within the cut-in and cut-out wind speeds of the NREL 5 MW OWT as indicated in Table 1, with a turbulence intensity of 12 %. The simulated time duration and interval are 500 s and 0.05 s, respectively. Fig. 8(a) illustrates the wind load (derived from the rotor) at the tower top under the cut-out wind speed of 25 m/s (Wind loads under the other three mean wind speeds are not presented here for conciseness).

The sea surface elevation is determined using the JONSWAP spectrum [62] in combination with the inverse fast Fourier transform. The Morison equation [62] is employed to calculate the sea wave loads acting on the monopile foundation. Two sea wave conditions are considered: a significant wave height of 6 m with a peak wave period of 10 s, and a significant wave height of 10 m with a peak wave period of 12.5 s. Fig. 8(b) shows the sea wave load at the SWL when the significant wave height and peak wave period are 6 m and 10 s, respectively.

6. Numerical results

The EHTNES is installed at the tower top to control the first mode of the OWT and harvest vibration energy in this study. The mass of EHTNES is assumed to be 3 % of the first modal mass, i.e., the mass ratio $\mu = 3$ %, and it is approximately 1.27×10^4 kg. With the natural frequency and damping ratio of the first mode of the OWT (i.e., 0.2810 Hz and 1 %, respectively), the EHTNES can be optimally designed on the basis of the method introduced in Subsection 2.4. However, k_1 and k_2 of the EHTNES cannot be solved simultaneously. Two steps are conducted: (1) assuming k_1 as zero to obtain k_2; (2) assuming k_2 as 1.5 times k_2 in (1) to obtain k_1. This assumption will be validated in the following subsection. Correspondingly, the stiffness and damping coefficients of the EHTNES are $k_1 = $ -19,043 N/m, $k_2 = $ 878,348 N/m^3, and $c_d = $ 3,763 N·s/m, respectively, unless otherwise.

The assumed EMD parameters include a machine constant K_{eq} of 245 N/A, parasitic damping c_p of 1,254 N·s/m (equivalent to 1/3 of the optimal damping), and a coil resistance R_{coil} of 3 Ω. In this scenario, optimal resistances for both vibration control and energy harvesting are identical, approximately 20 Ω, as indicated in Eqs. (16) and (20). These values serve as the basis for determining the parameters of the buck-boost EHC. Table 2 provides a summary of the corresponding circuit parameters to meet the on-demand damping. The modeling also considers the ESR of the electrical components. Fig. 9 depicts the Matlab Simulink model of the OWT-EHTNES system. The time step is set at 2×10^{-6} s to accommodate the high MOSFET switch frequency in the EHC.

As mentioned above, the dual-function performances of the EHTNES are compared with those of the EHTMD. For fair comparisons, the mass ratio of the EHTMD is the same as that of the EHTNES, and the optimal stiffness and damping coefficients are 38,085 N/m and 3,763 N·s/m, respectively (A similar Simulink model of the OWT-EHTMD is developed in this study but not presented here).

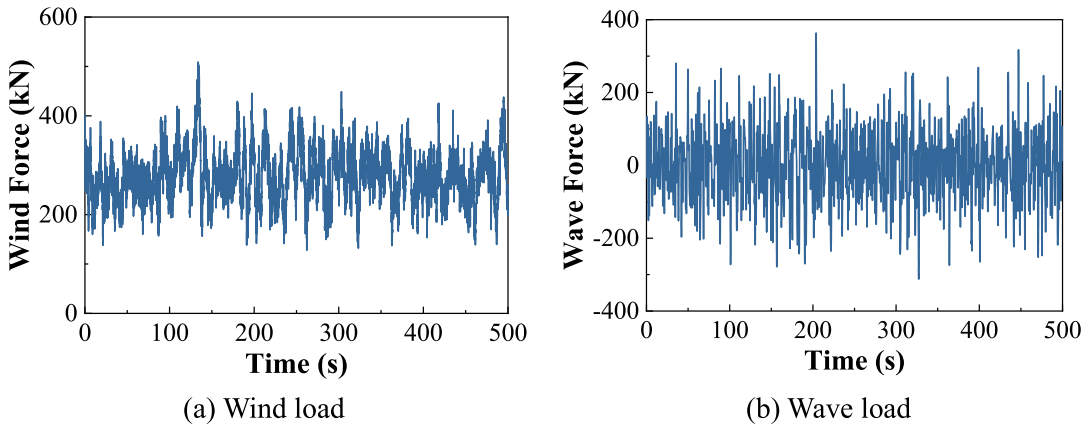

Fig. 8. Representative wind and wave loads.

Table 2
Main parameters of the numerical buck-boost EHC.

Parameters	Value	Parameters	Value
Input capacitor	240 μF	PWM wave duty cycle	44.9 %
ESR of input capacitor	0.2 Ω	MOSFET switch frequency	10 kHz
Output capacitor	10 μF	On-resistance of MOSFET	0.5 Ω
ESR of output capacitor	0.18 Ω	Battery voltage	110 V
Inductor	200 μH	Diode voltage drop	0.22 V
ESR of inductor	0.53 Ω		

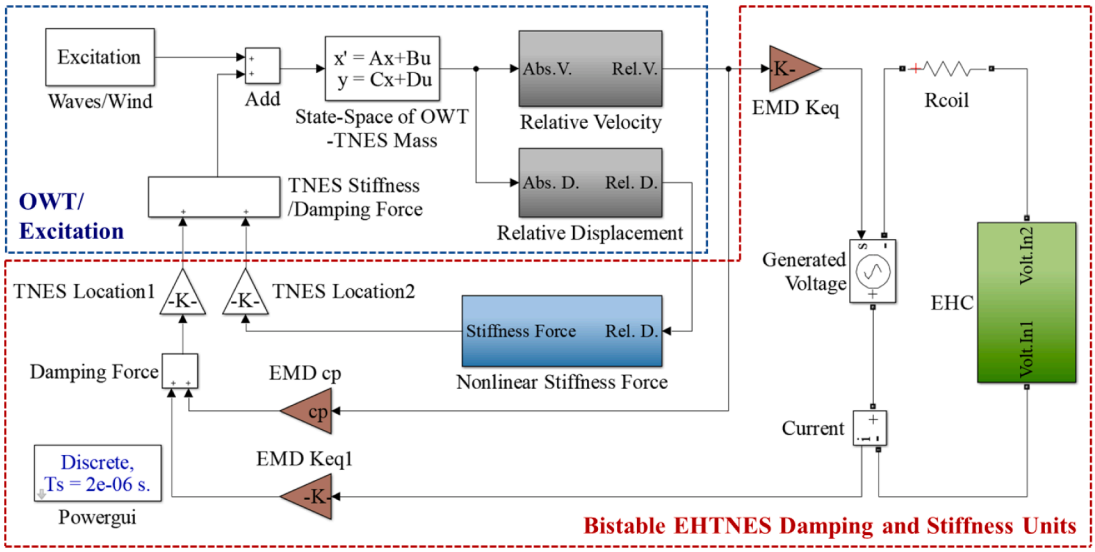

(a) OWT-EHTNES

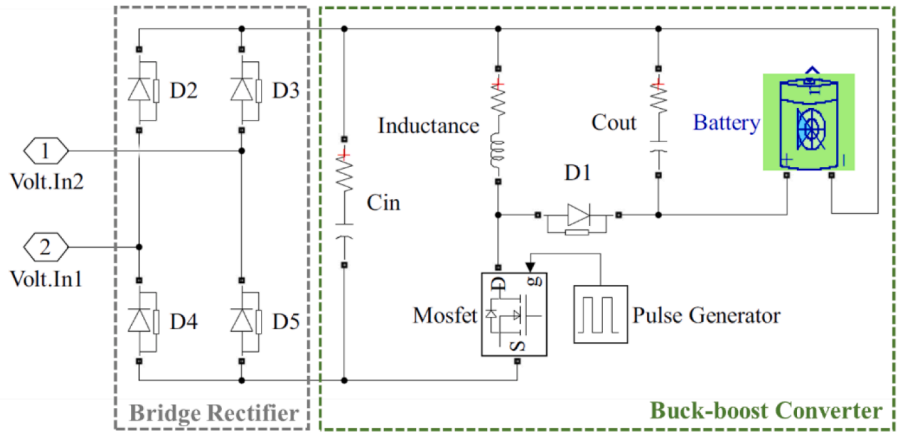

(b) Buck-boost EHC

Fig. 9. Matlab Simulink model of OWT-EHTNES.

6.1 Optimal validations

This subsection discusses the optimal parameters of the EHTNES when the OWT is subjected to a wind speed of 25 m/s, a significant wave height of 6 m, and a peak wave period of 10 s. Only the steady-state response (T = 100–500 s) is employed for the control and power analyses.

6.1.1. Stiffness coefficient

In the EHTNES design, k_2 is assumed as 1.5 times that of a cubic NES ($k_1 = 0$, $k_2 = 585{,}565$ N/m^3). To validate this assumption, the dual-function performances of the EHTNES are examined with k_2 varying in a range of [1,2] × 585,565 N/m^3 and k_1 varying in a range of [-1,0] × 38,085 N/m.

Fig. 10(a) shows the reduction ratios in displacement at the tower top when compared with the uncontrolled scenario. In this analysis, the standard deviation of displacement is adopted to eliminate the mean response. The EHTNES demonstrates consistent and stable reduction ratios in displacement, ranging from approximately 30 % to 36 % within the investigated range of stiffness coefficient. This finding indicates the effectiveness and robustness of the EHTNES. Fig. 10(b) presents the corresponding output power of the EHTNES, and it ranges from 140 W to 180 W. For comparison, the optimal EHTMD case is introduced. The optimal EHTMD exhibits superior dual functionality than the EHTNES, with improvements of roughly 10 % and 25 % in displacement reduction ratios and output power, respectively. However, the EHTMD commonly faces detuning issues in OWTs, leading to significant performance degradation [46,47].

6.1.2. Damping coefficient

The dual-function performances of the EHTNES under various damping coefficients are examined, where $c_d = (0.5 - 1.5) \times 3763$ N·s/m and the parasitic damping is fixed. Fig. 11 shows the displacement reduction ratios and output power. The variation in the EMD damping has limited effects on vibration control; the output power remains relatively stable with an increase in damping but generally decreases with decreased damping. Notably, the variation in the EMD damping influences both the vibration dynamics of the OWT and the power efficiency of the control devices. With fixed parasitic damping, lower EMD damping corresponds to lower power efficiency. In summary, the EHTNES has robust control and energy harvesting performances against the detuning stiffness and damping coefficients. In the following analyses, the stiffness and damping coefficients of the EHTNES are fixed at $k_1 = -19{,}043$ N/m, $k_2 = 878{,}348$ N/m^3, and $c_d = 3{,}763$ N·s/m.

6.2. Dual-function performances

The wind and wave loads are the same as those in Subsection 6.1, and this subsection specifically analyzes the dual-function performances of the EHTNES.

6.2.1. Vibration control performance

Figs. 12(a) and 13(a) show the displacement and acceleration time histories, respectively, at the tower top without control and with the EHTNES and EHTMD, and Figs. 12(b) and 13(b) are their corresponding power spectrum densities (PSDs) in the frequency domain, which can be obtained by using Welch's method [63] in Matlab. As shown, both the EHTNES and EHTMD dramatically reduce the OWT displacement and acceleration responses. The standard deviations of the displacements in 100–500 s are 0.092 m and 0.084 m for the EHTNES and EHTMD, respectively, which are much smaller than 0.140 m of the uncontrolled OWT, and the corresponding reduction ratios are 34 % and 40 %, respectively. Moreover, although the second-order vibration mode is observed in the acceleration responses, it is considerably smaller than the first-order mode. Both time and frequency domain results confirm the effectiveness of the EHTNES and EHTMD in vibration control. Notably, the reduction ratio achieved by the EHTNES is related to the mass ratio and the energy level of external excitations. As a passive control device, the control effectiveness of the EHTNES is notably contingent on the mass ratio between the EHTNES and the OWT. A large mass ratio generally enhances control effectiveness. In addition, previous research [64] has demonstrated that the effectiveness of nonlinear control devices is heavily dependent on the energy level of external excitations. Given the stochastic nature of wind and sea wave loads, the uncertain energy levels lead to varied reductions in the EHTNES under different wind and sea wave conditions.

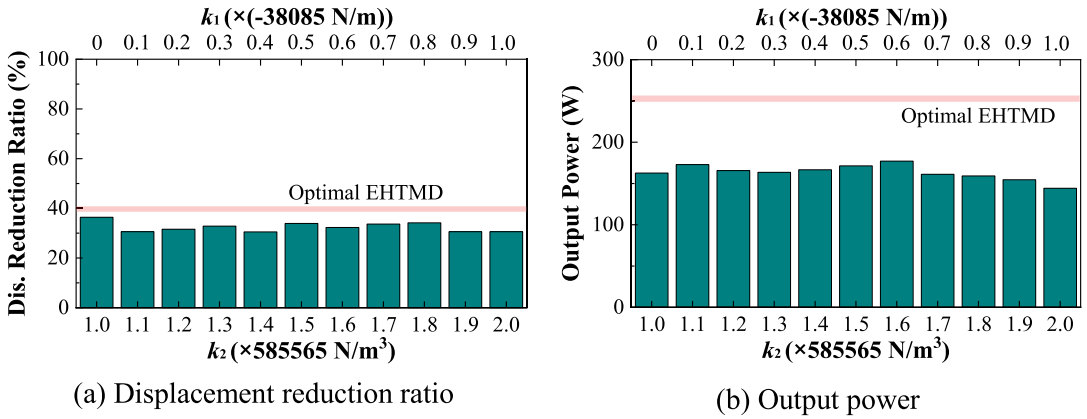

Fig. 10. Dual-function performances of EHTNES under various stiffness coefficients.

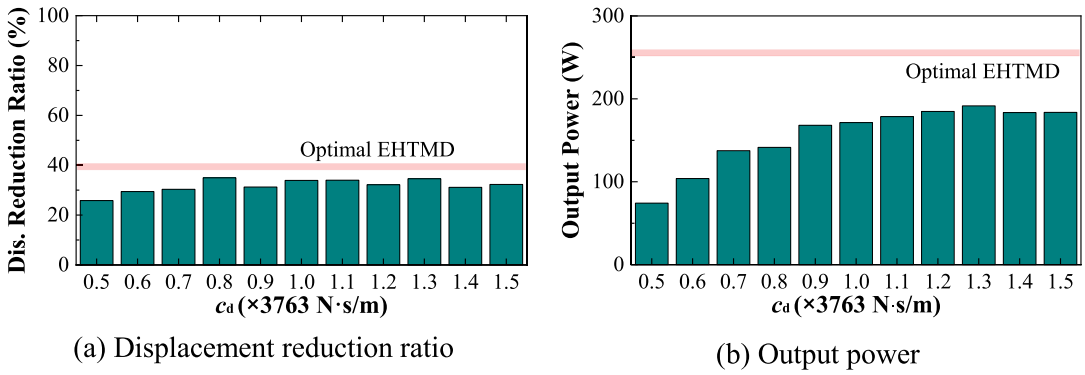

Fig. 11. Dual-function performances of EHTNES under various damping coefficients.

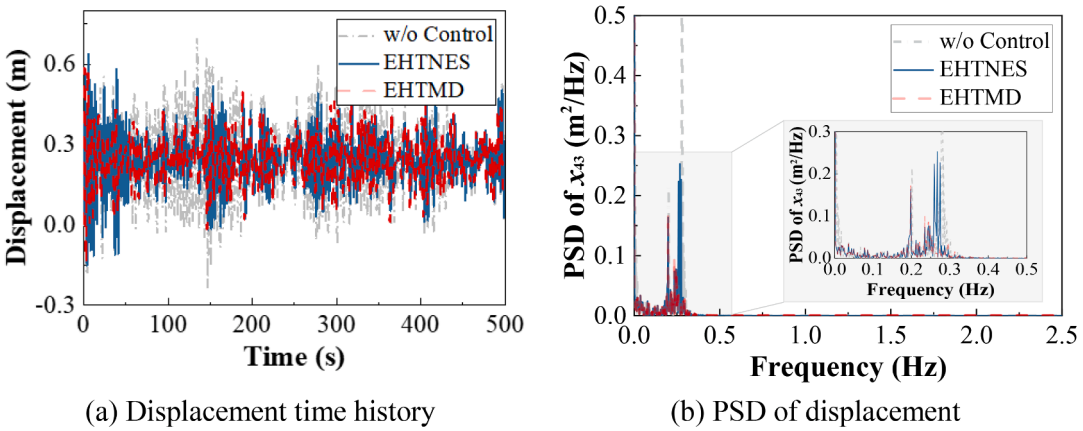

Fig. 12. Displacements and corresponding PSDs at the tower top.

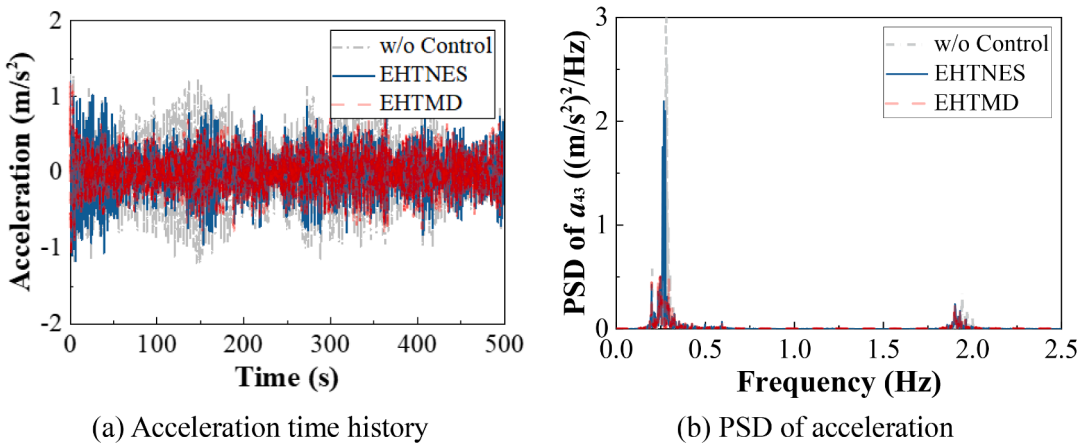

Fig. 13. Accelerations and corresponding PSDs at the tower top.

Fig. 14(a) illustrates the relationship between the damping force and the velocity, showcasing the EMD functions as a traditional viscous damper. The damping coefficient is roughly 3,893 N·s/m, closely aligning with the design value of 3,763 N·s/m, with a minimal error of 3 %. Fig. 14(b) and (c) show the displacement-velocity relationship and displacement time history of the EHTNES. Two equilibrium positions of the EHTNES are calculated by $\pm\left(-k_1/k_2\right)^{1/2} = \pm\ 0.147$ m, and they are marked by the red dots and dashed lines in Fig. 14(b) and (c), respectively. As shown, the EHTNES moves between two equilibrium positions, indicating its ability to overcome potential barriers and achieve bistability. However, the movement of the EHTNES is dependent on the intensity of

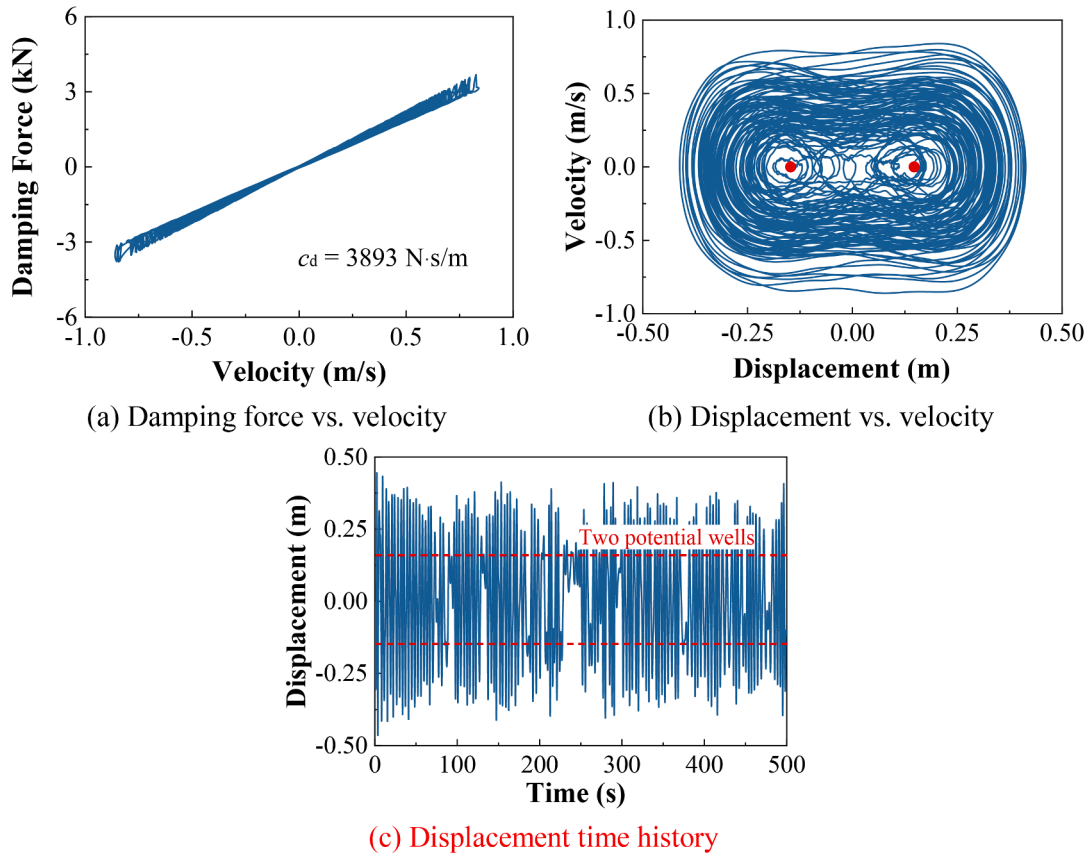

Fig. 14. Characterization of the EHTNES damping force, displacement, and velocity.

excitation. Under low excitation intensity, the EHTNES would oscillate around its equilibrium positions [64]. Notably, the displacement and velocity of the EHTNES in Fig. 14 are relative to those of the tower top. Moreover, the initial displacement and velocity of the EHTNES are zero. As mentioned above, only the steady-state response within 100–500 s is analyzed and discussed, except for the time history curves, implying that the damping force, velocity, and displacement presented in Fig. 14(a) and (b) are the results within the period of 100–500 s.

6.2.2. *Energy harvesting performance*

Fig. 15 illustrates the rectifier voltage and current of the buck-boost EHC in the period of 100 s to 110 s. In each switching cycle, the rectifier current experiences a drop to zero, mirroring the behavior seen in the energy-harvesting damping unit test (Section 3), indicating that the EHC is operating in DCM. The rectifier voltage consistently remains positive, which is attributed to the full-bridge rectifier function. The EHC equivalent resistance after the rectifier is approximately 19.7 Ω, aligning closely with the intended value of 20 Ω. Similar observations hold for the EHTMD.

Fig. 16 shows the power and efficiency characteristics of the EHTNES, and they are compared to the EHTMD. As shown, the first and second sub-efficiencies are estimated at 70.0 % and 86.3 %, respectively, reasonably aligning with the theoretical designs (Eqs. (18) and (19)), which predict the values of 66.6 % and 87.0 %, respectively. The power losses are primarily caused by parasitic damping and coil resistance. The third power efficiency stands at merely 67.8 % due to the ESR of electrical components and a relatively higher battery voltage. The power charged into the battery P_{out} is approximately 171 W, constituting nearly 41 % of the total damping power P_d. While the energy harvesting performance of the EHTMD surpasses that of the EHTNES, their efficiency trends are nearly identical due to the same optimal damping, EMD, and buck-boost EHC. Notably, the power output from the dual-function devices in this study is lower than the power generation rate of the OWT. Nonetheless, the harvested power proves to be sufficient for independently powering numerous lights or wireless sensors within the OWT tower. Typical wireless sensors and compact fluorescent lamps are reported to operate at the watt level [65,66]. Moreover, higher power output could be achieved under extreme wind conditions or increased wind speeds. These findings underscore the considerable potential for realizing self-powered monitoring or lighting systems within an OWT.

6.2.3. *Discussions*

Notably, the above analysis of the vibration control and energy harvesting performances is carried out under only one load sample

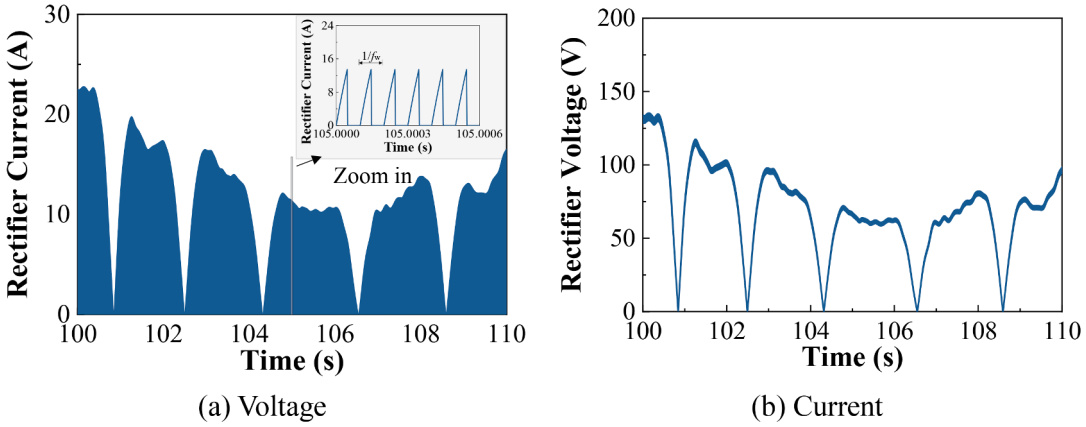

Fig. 15. Rectifier voltage and current of the buck-boost EHC.

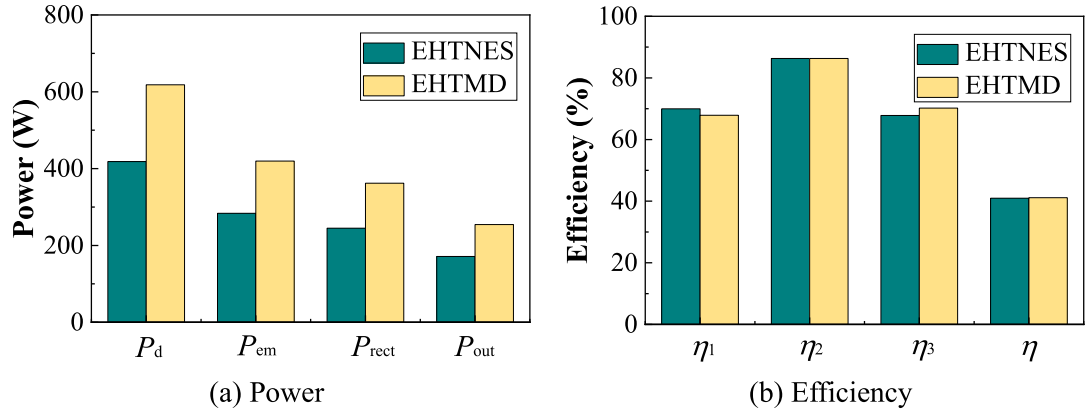

Fig. 16. Energy harvesting performance of the EHTNES and EHTMD.

of wind and sea wave. However, the same mean wind speed, significant wave height, and peak wave period are maintained; different wind and sea wave load time histories can be generated by employing different random seeds. To investigate the effect of stochastic wind and wave loads on the vibration control and energy harvesting performances of both the EHTNES and EHTMD, additional four sets of wind and wave loads are simulated. These simulations correspond to a mean wind speed of 25 m/s, a significant wave height of 6 m, and a peak wave period of 10 s. Notably, the present circuit topology adopts a time step of 2×10^{-6} s, and the computation time for a 500 s load time history is approximately 4 h. Therefore, only four additional time histories with one wind and wave condition are included.

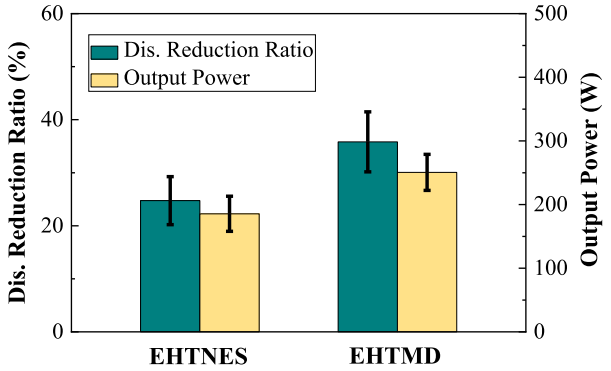

Fig. 17. Mean and standard error of displacement reduction ratio and output power.

Fig. 17 shows the mean and standard error of the displacement reduction ratio and output power of the EHTNES and EHTMD under the five wind and wave load samples. As expected, variations in the vibration control and energy harvesting performances are observed among these load samples. The average displacement reduction ratios of the EHTNES and EHTMD are approximately 25 % and 35 %, respectively, and their average output powers are approximately 185 W and 250 W, respectively. The observation is consistent with that in Subsections 6.1 and 6.2, where only one load sample is considered. Notably, the standard error in the reduction ratios and output power are anticipated to decrease with increased load samples and load generation time. Moreover, the variations in vibration control and energy harvesting performances are influenced not only by load uncertainty but also by uncertainties associated with the OWT and dual-function devices. A systematic exploration that considers uncertainties in the OWT, dual-function devices, and load would be valuable.

6.3. *Different combined wave-wind excitations*

This subsection outlines the dual-function performances of the EHTNES under diverse combined wind-wind excitations. Fig. 18(a) presents the reduction ratios of the standard deviations of the displacements at the tower top, ranging from approximately 14 % to 34 % in the investigated load cases. Notably, variations in significant wave heights and periods exert limited influence on the vibrations because the wave load is acting on the monopile foundation. Fig. 18(b) illustrates the corresponding output power performance of the EHTNES, showing an increase from 30 W to 170 W as the wind speed increases from 8 m/s to 25 m/s. These results further demonstrate the superior dual-function performances of the proposed EHTNES under complex wind-wave load conditions.

7. Conclusions

This study explores the feasibility of employing a bistable EHTNES in OWTs under combined wind and wave loads. It is the first study of simultaneous nonlinear vibration control and energy harvesting in OWTs, with deep insights into the coupling between OWTs and EHTNES. A detailed model of the bistable EHTENS is provided, and an experiment focusing on the energy-harvesting damping unit comprising an EMD and a buck-boost EHC was conducted to validate its damping and power performances. The application of the bistable EHTNES to a 5 MW OWT is exemplified. Its dual-function performances are investigated and compared with an EHTMD, considering parameter detuning issues and diverse combined wind-wave loads. The results showcase the ability of the bistable EHTNES to concurrently mitigate vibrations induced by combined wind-wave loads and facilitate energy harvesting in OWTs. This EHTNES can remarkably find application potentials in various structures, especially in offshore structures where power supply may pose challenges. The key findings can be summarized as follows:

(1) Through appropriate duty cycle selection, the buck-boost EHC functions as an equivalent constant energy-harvesting resistor. Consequently, the experimental energy-harvesting damping unit in the dual-function devices, including the bistable EHTNES, exhibits controllable damping effects and promising power generation performances.
(2) The vibration control effectiveness of the EHTNES is marginally inferior to the EHTMD, with an approximately 10 % degradation in displacement standard deviation. However, it is likely to demonstrate better robustness in designed parameter detuning.
(3) The mean output powers of the EHTNES under the rated and cut-out wind speeds are approximately 30 W and 170 W, respectively. These values are deemed sufficient for self-powered wireless sensors and fluorescent lamps in offshore structures. The output power of the EHTNES is relatively more sensitive to damping detuning than its vibration control effectiveness.

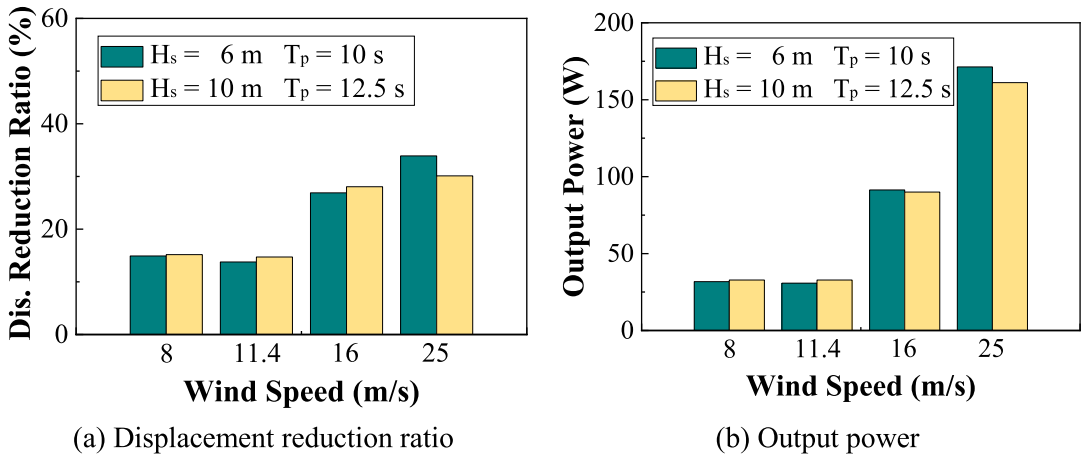

Fig. 18. Dual-function performances of the EHTNES under different wind-wave excitations (H_s and T_p are the significant wave height and peak wave period, respectively).

(4) The vibrations in monopile-foundation OWTs and the output power of the EHTNES have greater sensitivity to wind loads, whereas wave loads have limited effects.

This study experimentally validates the performance of the energy-harvesting damping unit (EMD plus EHC) in the EHTNES and numerically investigates the dual functionality of the EHTNES in an OWT. The prototype tests of a bistable EHTNES within a scaled OWT will be conducted in future work.

CRediT authorship contribution statement

Qinlin Cai: Writing – review & editing, Writing – original draft, Validation, Methodology, Funding acquisition, Conceptualization. **Yingyu Hua:** Validation, Data curation. **Songye Zhu:** Writing – review & editing, Supervision, Funding acquisition. **Xihong Zhang:** Writing – review & editing. **Haoran Zuo:** Writing – review & editing, Writing – original draft, Validation, Methodology, Funding acquisition, Conceptualization.

Declaration of competing interest

The authors declare that they have no known competing financial interests or personal relationships that could have appeared to influence the work reported in this paper.

Data availability

Data will be made available on request.

Acknowledgments

The authors would like to acknowledge the financial support from the National Natural Science Foundation of China (52208321 and 52108479), the Research Grants Council of Hong Kong through the NSFC/RGC CRS (No. CRS_PolyU503/23), and the Fundamental Research Funds for the Central Universities (No. YJ202405).

References

[1] H.B. Arsem, Electric shock absorber. (1971) U.S. Patent No. 3,559,027. https://patents.google.com/patent/US3559027A/en.
[2] Q. Cai, S. Zhu, The nexus between vibration-based energy harvesting and structural vibration control: A comprehensive review, Renew. Sust. Energ. Rev. 155 (2022) 111920, https://doi.org/10.1016/j.rser.2021.111920.
[3] K.F. Xu, Y.W. Zhang, J. Zang, M.Q. Niu, L.Q. Chen, Integration of vibration control and energy harvesting for whole-spacecraft: Experiments and theory, Mech. Syst. Signal Process. 161 (2021) 107956, https://doi.org/10.1016/j.ymssp.2021.107956.
[4] Y. Zhang, L. Wernicke, W. Wulff, A. Bleicher, T. Schauer, Design and validation of a dual-functional damper based on a stepper motor for energy harvesting and vibration control, Mech Syst Signal Process. 200 (2023) 110568, https://doi.org/10.1016/j.ymssp.2023.110568.
[5] R. Sun, W. Wong, L. Cheng, Bi-objective optimal design of an electromagnetic shunt damper for energy harvesting and vibration control, Mech. Syst. Signal Process. 182 (2023) 109571, https://doi.org/10.1016/j.ymssp.2022.109571.
[6] X. Xie, Q. Wang, Design of a piezoelectric harvester fixed under the roof of a high-rise building, Eng. Struct. 117 (2016) 1–9, https://doi.org/10.1016/j.engstruct.2016.03.018.
[7] R. Harne, Development and testing of a dynamic absorber with corrugated piezoelectric spring for vibration control and energy harvesting applications, Mech. Syst. Signal Process. 36 (2013) 604–617, https://doi.org/10.1016/j.ymssp.2012.10.012.
[8] S. Zhu, W. Shen, Y. Xu, Linear electromagnetic devices for vibration damping and energy harvesting: Modeling and testing, Eng. Struct. 34 (2012) 198–212, https://doi.org/10.1016/j.engstruct.2011.09.024.
[9] W. Shen, S. Zhu, Harvesting energy via electromagnetic damper: Application to bridge stay cables, J. Intell. Mater. Syst. Struct. 26 (2015) 3–19, https://doi.org/10.1177/1045389X13519003.
[10] D. Ning, H. Du, S. Sun, W. Li, W. Li, An energy saving variable damping seat suspension system with regeneration capability, IEEE Trans. Ind. Electron. 65 (2018) 8080–8091, https://doi.org/10.1109/TIE.2018.2803756.
[11] B. Yan, K. Wang, C.-X. Kang, X.N. Zhang, C.-Y. Wu, Self-sensing electromagnetic transducer for vibration control of space antenna reflector, IEEE ASME Trans. Mechatron. 22 (2017) 1944–1951, https://doi.org/10.1109/TMECH.2017.2712718.
[12] W. Shen, S. Zhu, H. Zhu, Experimental study on using electromagnetic devices on bridge stay cables for simultaneous energy harvesting and vibration damping, Smart Mater. Struct. 25 (2016) 065011, https://doi.org/10.1088/0964-1726/25/6/065011.
[13] Q. Cai, S. Zhu, Enhancing the performance of electromagnetic damper cum energy harvester using microcontroller: Concept and experiment validation, Mech. Syst. Signal Process. 134 (2019) 106339, https://doi.org/10.1016/j.ymssp.2019.106339.
[14] D. Ning, S. Sun, H. Du, W. Li, N. Zhang, Vibration control of an energy regenerative seat suspension with variable external resistance, Mech. Syst. Signal Process. 106 (2018) 94–113, https://doi.org/10.1016/j.ymssp.2017.12.036.
[15] X. Tang, L. Zuo, Simultaneous energy harvesting and vibration control of structures with tuned mass dampers, J. Intell. Mater. Syst. Struct. 23 (2012) 2117–2127, https://doi.org/10.1177/1045389X124626.
[16] Q. Cai, S. Zhu, S.T. Ke, Can we unify vibration control and energy harvesting objectives in energy regenerative tuned mass dampers? Smart Mater. Struct. 29 (2020) 087002 https://doi.org/10.1088/1361-665X/ab92de.
[17] W. Shen, A. Niyitangamahoro, Z. Feng, H. Zhu, Tuned inerter dampers for civil structures subjected to earthquake ground motions: optimum design and seismic performance, Eng. Struct. 198 (2019) 109470, https://doi.org/10.1016/j.engstruct.2019.109470.
[18] W. Shen, Z. Sun, Y. Hu, L. Cai, H. Zhu, S. Silva, Energy harvesting performance of an inerter-based electromagnetic damper with application to stay cables, Mech. Syst. Signal Process. 170 (2022) 108790, https://doi.org/10.1016/j.ymssp.2021.108790.
[19] W. Shen, S. Zhu, Y. Xu, An experimental study on self-powered vibration control and monitoring system using electromagnetic TMD and wireless sensors, Sens. Actuator A Phys. 180 (2012) 166–176, https://doi.org/10.1016/j.sna.2012.04.011.
[20] W. Shen, S. Zhu, Y.L. Xu, H. Zhu, Energy regenerative tuned mass dampers in high-rise buildings, Struct. Control Health Monit. 25 (2018) e2072.

[21] G. Caruso, G. Chirianni, G. Vairo, Energy harvesting from wind-induced bridge vibrations via electromagnetic transduction, Eng. Struct. 115 (2016) 118–128, https://doi.org/10.1016/j.engstruct.2016.02.020.
[22] S. Kopylov, Z. Chen, M.A. Abdelkareem, Implementation of an electromagnetic regenerative tuned mass damper in a vehicle suspension system, IEEE Access. 8 (2020) 110153–110163, https://doi.org/10.1109/ACCESS.2020.3002275.
[23] B. Yan, S. Zhou, C. Zhao, K. Wang, C. Wu, Electromagnetic energy harvester for vibration control of space rack: modeling, optimization, and analysis, J. Aerosp. Eng. 32 (2019) 04018126, https://doi.org/10.1061/(ASCE)AS.1943-5525.00009.
[24] V. Jahangiri, C. Sun, Integrated bi-directional vibration control and energy harvesting of monopile offshore wind turbines, Ocean Eng. 178 (2019) 260–269, https://doi.org/10.1016/j.oceaneng.2019.02.015.
[25] F. Qian, Y. Luo, H. Sun, W.C. Tai, L. Zuo, Optimal tuned inerter dampers for performance enhancement of vibration isolation, Eng. Struct. 198 (2019) 109464, https://doi.org/10.1016/j.engstruct.2019.109464.
[26] T. Asai, Y. Araki, K. Ikago, Structural control with tuned inertial mass electromagnetic transducers, Struct. Control Health Monit. 25 (2018) e2059.
[27] K. Sugiura, Y. Watanabe, T. Asai, Y. Araki, K. Ikago, Experimental characterization and performance improvement evaluation of an electromagnetic transducer utilizing a tuned inerter, J. Vib. Control 26 (2020) 56–72, https://doi.org/10.1177/1077546319876396.
[28] Q. Jin, X. Li, N. Sun, J. Zhou, J. Guan, Experimental and numerical study on tuned liquid dampers for controlling earthquake response of jacket offshore platform, Mar. Struct. 20 (2007) 238–254, https://doi.org/10.1016/j.marstruc.2007.05.002.
[29] R. Sardar, S. Chakraborty, Wave vibration control of jacket platform by tuned liquid dampers, Ocean Eng. 247 (2022) 110721, https://doi.org/10.1016/j.oceaneng.2022.110721.
[30] R. Ma, K. Bi, H. Hao, Heave motion mitigation of semi-submersible platform using inerter-based vibration isolation system (IVIS), Eng. Struct. 219 (2020) 110833, https://doi.org/10.1016/j.engstruct.2020.110833.
[31] R. Ma, K. Bi, H. Zuo, X. Du, Inerter-based damping isolation system for vibration control of offshore platforms subjected to ground motions, Ocean Eng. 280 (2023) 114726, https://doi.org/10.1016/j.oceaneng.2023.114726.
[32] H.H. Lee, H. Juang, Experimental study on the vibration mitigation of offshore tension leg platform system with UWTLCD, Smart Struct. Syst. 9 (2012) 71–104.
[33] R. Kandasamy, F. Cui, N. Townsend, C.C. Foo, J. Guo, A. Shenoi, Y. Xiong, A review of vibration control methods for marine offshore structures, Ocean Eng. 127 (2016) 279–297, https://doi.org/10.1016/j.oceaneng.2016.10.001.
[34] B.L. Zhang, Q.L. Han, X.M. Zhang, Recent advances in vibration control of offshore platforms, Nonlinear Dyn. 89 (2017) 755–771, https://doi.org/10.1007/s11071-017-3503-4.
[35] H. Zuo, K. Bi, H. Hao, Simultaneous out-of-plane and in-plane vibration mitigations of offshore monopile wind turbines by tuned mass dampers, Smart Struct. Syst. 26 (2020) 435–449, https://doi.org/10.12989/sss.2020.26.4.435.
[36] C. Sun, V. Jahangiri, Bi-directional vibration control of offshore wind turbines using a 3D pendulum tuned mass damper, Mech. Syst. Signal Process. 105 (2018) 338–360, https://doi.org/10.1016/j.ymssp.2017.12.011.
[37] Z. Zhang, B. Basu, S.R. Nielsen, Real-time hybrid aeroelastic simulation of wind turbines with various types of full-scale tuned liquid dampers, Wind Energy. 22 (2019) 239–256, https://doi.org/10.1002/we.2281.
[38] S. Colwell, B. Basu, Tuned liquid column dampers in offshore wind turbines for structural control, Eng. Struct. 31 (2009) 358–368, https://doi.org/10.1016/j.engstruct.2008.09.001.
[39] G. Liu, Z. Lei, H. Wang, Investigation and optimization of a pre-stressed tuned mass damper for wind turbine tower, Struct. Control Health Monit. 29 (2022) e2894.
[40] X. Liu, J. Xu, G. He, C. Chen, Lateral vibration mitigation of monopile offshore wind turbines with a spring pendulum pounding tuned mass damper, Ocean Eng. 266 (2022) 112954, https://doi.org/10.1016/j.oceaneng.2022.112954.
[41] M.Z. Chen, Z. Li, H. Wang, Y. Hu, Seismic response mitigation of a wind turbine via inerter-based structural control, Bull. Earthq. Eng. 21 (2023) 1361–1388, https://doi.org/10.1007/s10518-021-01267-x.
[42] R. Zhang, Z. Zhao, K. Dai, Seismic response mitigation of a wind turbine tower using a tuned parallel inerter mass system, Eng. Struct. 180 (2019) 29–39, https://doi.org/10.1016/j.engstruct.2018.11.020.
[43] P.G. Wang, H.Q. Lu, M. Wang, S. Nagarajaiah, X.L. Du, Experimental and numerical investigations on seismic responses of wind turbine structures with amplifying damping transfer system, Soil. Dyn. Earthq. Eng. 175 (2023) 108277, https://doi.org/10.1016/j.soildyn.2023.108277.
[44] M. Ghassempour, G. Failla, F. Arena, Vibration mitigation in offshore wind turbines via tuned mass damper, Eng. Struct. 183 (2019) 610–636, https://doi.org/10.1016/j.engstruct.2018.12.092.
[45] L. Wang, W. Zhou, Z. Guo, S. Rui, Frequency change and accumulated inclination of offshore wind turbine jacket structure with piles in sand under cyclic loadings, Ocean Eng. 217 (2020) 108045, https://doi.org/10.1016/j.oceaneng.2020.108045.
[46] K. Dai, H. Huang, Y. Lu, J. Meng, Z. Mao, A. Camara, Effects of soil–structure interaction on the design of tuned mass damper to control the seismic response of wind turbine towers with gravity base, Wind Energy. 24 (2021) 323–344, https://doi.org/10.1002/we.2576.
[47] G.L. Lin, L.Y. Lu, K.T. Lei, K.Y. Liu, Y.Y. Ko, S.H. Ju, Experimental study on seismic vibration control of an offshore wind turbine with TMD considering soil liquefaction effect, Mar. Struct. 77 (2021) 102961, https://doi.org/10.1016/j.marstruc.2021.102961.
[48] H. Ding, L.Q. Chen, Designs, analysis, and applications of nonlinear energy sinks, Nonlinear Dyn. 100 (2020) 3061–3107, https://doi.org/10.1007/s11071-020-05724-1.
[49] Z. Lu, Z. Wang, Y. Zhou, X. Lu, Nonlinear dissipative devices in structural vibration control: A review, J. Sound Vib. 423 (2018) 18–49, https://doi.org/10.1016/j.jsv.2018.02.052.
[50] J. Wang, N.E. Wierschem, B.F. Spencer Jr, X. Lu, Track nonlinear energy sink for rapid response reduction in building structures, J. Eng. Mech. 141 (2015) 04014104, https://doi.org/10.1061/(ASCE)EM.1943-7889.0000824.
[51] H. Zuo, S. Zhu, Development of novel track nonlinear energy sinks for seismic performance improvement of offshore wind turbine towers, Mech Syst Signal Process. 172 (2022) 108975, https://doi.org/10.1016/j.ymssp.2022.108975.
[52] H. Zuo, J. Zhang, G.K. Yuan, S. Zhu, Wind-and sea wave-induced response mitigations of offshore wind turbines using track nonlinear energy sinks, Struct. Control Health Monit. 29 (2022) e2990.
[53] H. Zuo, J. Zhang, K. Bi, S. Zhu, H. Hao, R. Ma, Structural vibration control of spar-buoy floating offshore wind turbines, Eng. Struct. 294 (2023) 116732, https://doi.org/10.1016/j.engstruct.2023.116732.
[54] P.D. Mitcheson, T.T. Toh, K.H. Wong, S.G. Burrow, A.S. Holmes, Tuning the resonant frequency and damping of an electromagnetic energy harvester using power electronics, IEEE Trans, Circuits Syst. II Express Briefs. 58 (2011) 792–796, https://doi.org/10.1109/TCSII.2011.2173966.
[55] Q. Cai, Y. Hua, S. Zhu, Energy-harvesting adaptive vibration damping in high-speed train suspension using electromagnetic dampers, Int. J. Struct. Stab. Dyn. 21 (2021) 2140002, https://doi.org/10.1142/S0219455421400022.
[56] M. Oliva, G. Barone, G. Navarra, Optimal design of nonlinear energy sinks for SDOF structures subjected to white noise base excitations, Eng. Struct. 145 (2017) 135–152, https://doi.org/10.1016/j.engstruct.2017.03.027.
[57] Y. Hua, Q. Cai, S. Zhu, Energy-regenerative semiactive lateral suspension control in high-speed trains using electromagnetic damper cum energy harvester, IEEE Trans. Veh. Technol. 71 (2022) 4801–4812, https://doi.org/10.1109/TVT.2022.3149265.
[58] J. Jonkman, S. Butterfield, W. Musial, G. Scott, Definition of a 5-MW reference wind turbine for offshore system development (No. NREL/TP-500-38060), Nat. Renew. Energy Labo. (NREL) (2009), https://doi.org/10.2172/947422. Golden, Colorado (United States).
[59] J.Y. Li, S. Zhu, J. Zhang, R. Ma, H. Zuo, Vibration control of offshore wind turbines with a novel energy-adaptive self-powered active mass damper, Eng. Struct. 302 (2024) 117450, https://doi.org/10.1016/j.engstruct.2024.117450.
[60] IEC 61400–1, Wind turbines-Part 1: Design requirements, 3rd ed., International Electrotechnical Commission, Geneva, Switzerland, 2005.
[61] P.J. Moriarty, H.A. Craig, AeroDyn Theory Manual (No. NREL/EL-500-36881), Nat. Renew. Energy Lab. (2005). Golden, Colorado (United States).

[62] Det Norske Veritas (DNV). DNV-RP-C205: Environmental conditions and environmental loads. DNV, Norway, 2010. https://www.dnv.com/oilgas/download/dnv-rp-c205-environmental-conditions-and-environmental-loads.html.
[63] P. Welch, The use of fast Fourier transform for the estimation of power spectra: a method based on time averaging over short, modified periodograms, IEEE Trans. Audio Electroacoust. 15 (2) (1967) 70–73, https://doi.org/10.1109/TAU.1967.1161901.
[64] H. Zuo, K. Bi, S. Zhu, R. Ma, H. Hao, On the dynamic characteristics of using track nonlinear energy sinks for structural vibration control, Eng. Struct. 302 (2024) 117436, https://doi.org/10.1016/j.engstruct.2023.117436.
[65] L. Guan, T. Berrill, R.J. Brown, Measurement of actual efficacy of compact fluorescent lamps (CFLs), Energy Build. 86 (2015) 601–607, https://doi.org/10.1016/j.enbuild.2014.10.068.
[66] J.P. Lynch, K.H. Law, A.S. Kiremidjian, E. Carryer, C.R. Farrar, H. Sohn, D.W. Allen, B. Nadler, J.R. Wait, Design and performance validation of a wireless sensing unit for structural monitoring applications, Struct. Eng. Mech. 17 (2004) 393–408, https://doi.org/10.12989/sem.2004.17.3_4.393.